Materials Futures

PAPER • OPEN ACCESS

Vacancy-engineered $LiMn_2O_4$ embedded in dual-heteroatom-doped carbon via metal-organic framework-mediated synthesis towards longevous lithium ion battery

To cite this article: Xiaoming Lin *et al* 2025 *Mater. Futures* **4** 025101

OPEN ACCESS
IOP Publishing | Songshan Lake Materials Laboratory

MATERIALS FUTURES

Mater. Futures 4 (2025) 025101 (15pp)

https://doi.org/10.1088/2752-5724/ad9e08

Vacancy-engineered $LiMn_2O_4$ embedded in dual-heteroatom-doped carbon via metal-organic framework-mediated synthesis towards longevous lithium ion battery

Xiaoming Lin[1,*], Jia Lin[1], Xiaomeng Lu[2], Xiaohong Tan[1], Hao Li[2], Wanxin Mai[1], Yuhong Luo[1], Yongbo Wu[3,4], Shuangqiang Chen[2], Chao Yang[2,*] and Yong Wang[2,*]

[1] School of Chemistry, South China Normal University, Guangzhou 510006, People's Republic of China
[2] School of Environmental and Chemical Engineering, Shanghai University, Shanghai 200444, People's Republic of China
[3] Key Laboratory of Atomic and Subatomic Structure and Quantum Control (Ministry of Education), Guangdong Basic Research Center of Excellence for Structure and Fundamental Interactions of Matter, School of Physics, South China Normal University, Guangzhou 510006, People's Republic of China
[4] Guangdong Provincial Key Laboratory of Quantum Engineering and Quantum Materials, Guangdong-Hong Kong Joint Laboratory of Quantum Matter, South China Normal University, Guangzhou 510006, People's Republic of China

E-mail: linxm@scnu.edu.cn, chaoyang@shu.edu.cn and yongwang@shu.edu.cn

Received 20 September 2024, revised 21 November 2024
Accepted for publication 8 December 2024
Published 3 March 2025

Abstract

Spinel $LiMn_2O_4$ (LMO) is deemed to be a promising cathode material for commercial lithium-ion batteries (LIBs) in prospect of its cost-effectiveness, nontoxicity, fabulous rate capability, and high energy density. Nevertheless, the LMO is inevitably confronted with sluggish diffusion kinetics and drastic capacity degradation triggered by multiple issues, including Jahn–Teller distortion, Mn dissolution, and structural attenuation. Thereinto, a metal-organic framework (MOF) chemistry engineering for hierarchical micro-/nano-structural F, O-dual-doped carbon embedded oxygen vacancy enriched $LiMn_2O_4$ cathode (O_V-LMO@FOC) is proposed for longevous LIBs. Bestowed by experimental and theoretical implementations, systematic investigations of O_V-LMO@FOC endow that the meticulous integration of F, O-dual-doped carbon and oxygen vacancy in LMO-based cathode reconfigures the electronic structure, boosts electronic conductivity, expedites diffusion capability, facilitates energetically preferable Li^+ adsorption, and suppresses Mn dissolution in the electrolyte, consequently achieving fabulous long-term cycling stability. As expected, the O_V-LMO@FOC behaves with compelling electrochemical performance with prosperous reversible capacity (130.2 mAh g^{-1} at 0.2 C upon 200 cycles), exceptional rate capacity (93.7 mAh g^{-1} even at

* Authors to whom any correspondence should be addressed.

20 C), and pronounced long-term cyclability (112.5 mAh g^{-1} after 1200 cycles with 77.6% capacity retention at 1 C). Even at the ultrahigh current density of 5 C, the O_V-LMO@FOC bears a brilliant capacity of 96.9 mAh g^{-1} upon 1000 cycles with an extraordinary capacity retention of 90.7%, and maintains a discharge capacity of 70.9 mAh g^{-1} upon 4000 cycles. This work envisions the MOF-chemistry in surface modification and electronic modulation engineering of high-performance cathode materials towards industrialization in automotive market.

Supplementary material for this article is available online

Keywords: metal-organic framework, spinel $LiMn_2O_4$ cathode, oxygen vacancy engineering, dual-heteroatom-doped carbon, longevous lithium ion battery

1. Introduction

With the global intensification of carbon neutrality and surging popularity of electric vehicles (EVs), the development of electrode technology has been flourishing to intrigue the competitive electrochemical metrics (cost-efficiency, energy density, and cycling lifespan) of lithium-ion batteries (LIBs) upon the electrification of automobile industry [1]. Cathode materials are arguably commensurate with more than 40% of both cost and energy density of LIB system [2]. The olivine lithium iron phosphates ($LiFePO_4$, LFP), layered lithium metal oxides ($LiNi_xCo_yMn_zO_2$, NCM, $x + y + z = 1$), and spinel lithium manganese oxides ($LiMn_2O_4$, LMO) are aggressively used as the commercialized cathode materials [3, 4]. Among them, the LFP delivers low operating voltage (~3.4 V) and limited energy-density level despite of its low cost; while the NCM cathodes involve the controversial transition-metal elements of Ni and Co, encountering with the reserve depletion, localized supply, high value, and toxicity, which impedes their industrialization of EVs [5, 6]. Alternatively, the all-manganese-based LMO endows the advantage complementary of environmental compatibility, high thermal stability, nontoxicity, high voltage (~4 V), high energy density and safety, as well as overwhelming cost superiority (the price of manganese is approximately 20% of Ni and below 10% of Co) [7]. Nevertheless, the LMO cathode is mainly plagued by the cubic-tetragonal Jahn–Teller distortion, Mn^{2+} dissolution in electrolyte due to the Mn^{3+} disproportionation mechanism, jeopardizes the electrode polarization and long-term cyclability, thus leading to severe capacity degradation upon electrochemical operation [8, 9].

To tackle the above conundrum, orchestrated efforts have been focused on modification engineering, concerning chemical bulk doping, surface coating, morphological manipulation, and structural design, to mitigate the capacity decline of LMO [10, 11]. Nevertheless, the single micro- or nanostructure might accordingly compensate for the rate capability or tap density of LMO cathode materials, which is still a challenge for scale-up applications. It intrigues versatile micro-/nano-structural design for cathode chemistry with pronounced rate performance and energy density, which can integrate not only high tap density from microstructure but also the superior rate performance from nanostructure [12, 13]. As for compositional optimization, the heteroatom-doping in LMO bulk might result in new configuration [14]. Hence, surface modification is deemed as an effective approach by coating materials (such as oxides [15], phosphates [16], fluorides [17], conductive carbons [18], etc). Embedding cathode materials into carbonaceous matrix exerts non-negligible influence on boosting electronic conductivity, suppressing electrode polarization, mitigating direct contact between electrolyte and Mn^{3+}, and ameliorating Mn dissolution in the electrolyte [19–21]. The elastic carbon matrix not only serves as protective layer to immobilize the structure variation of LMO, electroactive particle agglomeration, and electrolyte corrosion upon (de)lithiation, but also provides tremendous extra lithium storage sites towards exalted rate performance [22, 23]. Whilst, it is of note that anionic heteroatom-doping (such as F, N, S, P, etc) carbon can provide extra defective and active sites for lithium storage [24, 25]. It is acknowledged that fluorine serves as the most electronegative element and characters compelling electronegativity, facilitating manipulated electronic properties and ameliorating interfacial resistance. Hence, F doping is a promising strategy for the improvement of LMO in electronic conductivity due to the much stronger electronegativity of F compared with other heteroatoms [25]. Unfortunately, conventional F-doping strategy requires harsh synthetic conditions by F_2 or XeF_2 flow fluorination [26], which is difficult to implement in experimental studies and may cause environmental hazards. Taking 'green chemistry' appeal and the necessity of F doping into account, a delicate protocol by facile solvothermal/solid-state reactions for micro-/nano-structural dual-heteroatom-doped carbon embedded spinel $LiMn_2O_4$ cathode is instrumental in optimizing the long-term cycle stability with integrated energy density.

Given the appealing inorganic-organic chemistry, abundant distributed active sites, and hierarchical designed structure, metal-organic frameworks (MOFs) interconnected polytopic organic linkers with metal-centered nodes (single-metal nodes or polynuclear clusters), are recognized as the mainstream of periodically porous templates for MOF-derived dual-heteroatom-doped carbon embedded materials [27, 28]. It is conducive to the uniform distribution/coating of carbonaceous surface coating materials with electroactive LMO bulk,

which mitigates the direct contact between LMO and corrosive electrolyte, parasitic side reaction of Mn^{3+} disproportionation and Jahn–Teller effect. Impressively, MOF-mediated synthesis strategy has been spotlighted as the feasible and mild methodology for oxygen vacancies (O_V) engineering by sintering under simple oxygen-poor conditions (such as N_2 or Ar atmosphere) to self-adaptively manipulate the local electronic structure without radically changing pristine lattice [29]. During this synthetic route, high-temperature sintering under reductive atmospheres is energetically favorable for oxygen vacancy formation and can simultaneously warrant the crystallinity degree of the LMO products. The local built-in electric field induced by the introduction of O_V is conducive to optimizing the electrochemical performance with more electroactive sites, boosting lithium ion diffusivity, decreasing energy barrier, and suppressing structural deformation upon repeated (de)lithiation process [30, 31]. Whereas, the MOF engineering for constructing carbon embedded $LiMn_2O_4$ is still in its infant stage, which might facilitate the lithium storage metrics to confer MOF-chemistry penetration into automotive-type lithium ion battery cathode.

By leveraging the aforementioned complementarity, herein, we elaborately design and fabricate a MOF-chemistry engineering for hierarchical micro-/nano-structural F, O-dual-doped carbon embedded spinel $LiMn_2O_4$ cathode (hereinafter termed as O_V-LMO@FOC) by solvothermal and high-temperature sintering methodologies as LIB cathode. Combining experimental and theoretical analyses, comprehensive investigations of O_V-LMO@FOC unveil that the uniformity and existence of oxygen vacancy and F, O-dual-doped carbon energetically facilitate Li^+ adsorption and diffusion capability, boost electronic conductivity, suppress Mn dissolution in electrolyte, further improving fabulous long-term cycling stability. Consequently, compelling electrochemical metrics are achieved with superior specific capacity, distinguished rate capacity, and exceptional cyclability. We envision that this work highlights the MOF-chemistry in surface modification engineering of high-performance cathode materials towards industrialization.

2. Experimental

2.1. Synthesis of O_V-LMO@FOC, O_V-LMO@OC, and LMO

In a typical synthetic protocol, 15 g of polyvinylpyrrolidone (PVP, K30, $M_w = 40\ 000$) and 2.45 g of $Mn(Ac)_2 \cdot 2H_2O$ were decentralized in 100 ml mixed solvent of ethanol and distilled water (EtOH: DI, 1: 1, vol%) via ultrasonic dispersion to obtain the solution A. 4.5 g of trimesic acid was decentralized in 100 ml mixed solvent of ethanol and distilled water (EtOH: DI, 1: 1, vol%) via ultrasonic dispersion to obtain the solution B. Then, the solution B was dropwise added into the solution A with vigorous magnetic stirring for another 30 min at room temperature, and further aged at room temperature for 24 h. The resulting precipitates were obtained by centrifuging and rinsing by ethanol for three times, and drying at 70 °C in the vacuum oven for 24 h.

The O_V-LMO@FOC was prepared via a Mn-MOF-mediated sintering treatment methodology. 1 g of Mn-MOF, 0.12 g of Li_2CO_3, and 0.12 g of NH_4F were uniformly mixed for 10 min in a mortar. Afterwards, the grounded precursors were sintered at 500 °C for 4 h under Ar atmosphere with a temperature ramping rate of 2 °C min^{-1} in a tubular furnace, and then sintered at 800 °C under Ar atmosphere with a temperature ramping rate of 4 °C min^{-1} for another 2 h. After naturally cooling to room temperature, the O_V-LMO@FOC was obtained.

Additionally, the O_V-LMO@OC was prepared in the similar way without adding NH_4F. Whereas the LMO was synthesized by sintering the mixture of Mn-MOF and Li_2CO_3 at 500 °C for 4 h in air, and then sintered at 800 °C under Ar atmosphere with a temperature ramping rate of 4 °C min^{-1} for another 2 h.

2.2. Morphological and structural characterization

The crystal structure and phase information were collected by x-ray diffraction (XRD, Ultima IV, Cu Kα radiation) using a scanning angle of 10−90°. The nitrogen adsorption/desorption isotherms (Micromeritics ASAP 2010, USA) at 77 K were conducted to specific surface area and pore size. Thermogravimetric analysis (TGA, NETZSCH TG 209 F1 Libra) from 30 to 800 °C with a heating rate of 10 °C min^{-1} under N_2 atmosphere. The elemental configuration and chemical valence states were characterized via x-ray photoelectron spectroscopy (XPS, Thermo Scientific K-Alpha$^+$) using Al Kα x-ray source. The morphological structure was obtained by Raman spectra (Renishaw inVia) via an argon ion laser beam. Surface morphology and microstructure were observed by scanning electron microscopy (SEM, FEI Quanta 250 FEG) and transmission electron microscopy (TEM, FEI Talos F200X) with high-angle annular dark-field (HAADF) STEM and energy dispersive x-ray spectrometer.

2.3. Electrochemical measurements

The active material, acetylene black, and polyvinylidene fluoride were mixed in the mass ratio of 7:2:1, and then decentralized in the appropriate amount of *N*-methylpyrrolidone solvent to prepare a syrupy mixture, which was further coated on Al foil current collector as cathode films and further dried at 110 °C in the vacuum oven for 20 h. Lithium foil was employed as the counter-electrode, Celgard 2500-type membrane was applied as the separator, and 1 M $LiPF_6$ dissolved in a mixture of ethylene carbonate, dimethyl carbonate, and diethyl carbonate organic solvents (EC: DMC: DEC, 1: 1: 1, vol%) was functioned as the electrolyte for cell assembly. The electrochemical properties of O_V-LMO@FOC, O_V-LMO@OC, and LMO cathodes were investigated by the assembled CR2032 coin-type cells, where the assemble process of the cells was conducted in the argon-filled glove box (Mikrouna, $H_2O \leqslant 0.1$ ppm, $O_2 \leqslant 0.1$ ppm). The mass loading of the active material for typical electrodes was ~2.54 mg cm^{-2}. Afterwards, the galvanostatic (dis)charge

(GCD) cycling tests were systematically performed by LAND 3001 A battery testing system at room-temperature within the potential range of 3−4.5 V at various rate densities (1 C = 148 mAh g^{-1}). The cyclic voltammetry (CV) with different sweep rates between 3−4.5 V and the electrochemical impedance spectroscopy (EIS) in the frequency range from 10^5 kHz to 10^{-2} Hz with the AC signal amplitude of 5 mV at room temperature were measured via the electrochemical workstation (CHI760E).

2.4. Calculation methods

The density functional theory (DFT) calculations were implemented by the Vienna *Ab-initio* Simulation Package [32] with the frozen-core all-electron projector-augment-wave [33] methodology. The Perdew–Burke–Ernzerhof [34] of generalized gradient approximation was employed to depict the exchange and correlation potential. The kinetic energy cutoff of 520 eV for the plane-wave basis set was considered. Grimme's DFT-D3 methodology was used to describe the dispersion interactions. The geometry optimizations were stopped upon the forces on each ion was lower than 0.03 eV $Å^{-1}$. The 3 × 3 × 1 Monkhorst-Pack k-pointsampling of the Brillouin zone was applied. The adsorption energies (ΔE_{ads}) were obtained by the equation: $\Delta E_{ads} = E_{Li+surface} - 8E_{surface} - E_{Li}$, where $E_{surface}$, E_{Li}, $E_{Li+surface}$ represent the energy of the LMO (111) slab and O_V-LMO@FOC (111) composite, the energy of the Li^+, and the total energy of the adsorbed system.

3. Results and discussions

Figure 1 schematically illustrates the preparation strategy for MOF-mediated O_V-LMO@FOC. Herein, the spherical Mn-MOF was assembled by trimesic acid and Mn^{2+}, and figure S1 shows the XRD pattern to confirm the successful fabrication and phase purity of Mn-MOF. The TGA curve reveals the thermal stability of Mn-MOF (figure S2). To prepare the O_V-LMO@FOC, the Mn-MOF, ammonium fluoride, and lithium carbonate were homogeneously mixed and further sintering in argon flow via solid-state sintering strategy, among which the lithium carbonate and Mn ions of Mn-MOF render as lithium and manganese source to form the $LiMn_2O_4$, respectively. Additionally, the trimesic acid ligand of Mn-MOF transforms into the carbon layer and the ammonium fluoride as etching reagent contributes to the fluorine dopants into the carbon matrix. The hierarchical MOF-mediated $LiMn_2O_4$ embedded in O-doped carbon (O_V-LMO@OC, without NH_4F) micro/nanoparticles and MOF-mediated $LiMn_2O_4$ (LMO, without NH_4F and sintering in air flow) were implemented as parallel experiments to investigate the electrochemical properties of O_V-LMO@FOC.

The morphological and crystal structures of O_V-LMO@FOC were observed by the SEM and TEM techniques. As shown in figures 2(a)–(c), the micro-sized spheres are consisted of tremendous nano-sized subunits, further leading to the hierarchical micro-/nano-structure of O_V-LMO@FOC. Worth mentioning, the O_V-LMO@FOC well-maintains the spherical hollow shape of the Mn-MOF template (figure S3), and has negligible difference with the O_V-LMO@OC after fluoridation (figure S4), which could be ascribed to the MOF-derived carbon matrix functioning as the template and structure protector for the Mn-MOF precursor morphology. The TEM image in figure 2(d) reveals that the hollow cavity inside micro-sized spheres can be observed in O_V-LMO@FOC, demonstrating the hierarchical hollow micro-/nano-architecture. Furthermore, the nano-sized $LiMn_2O_4$ subunits are coated with a ∼1.5 nm carbon layer (figure 2(e)), which could effectively avoid severe volume variation of LMO particles and the direct contact between LMO and electrolyte. Such a hierarchical hollow micro-/nano-architecture is conducive to improved electronic conductivity, extra lithium-ion storage sites, and alleviated volumetric expansion upon (dis)charge course [35]. According to figure S5, the average particle sizes of the primary $LiMn_2O_4$ particle for O_V-LMO@OC and O_V-LMO@FOC were calculated as ∼40.2 nm. Moreover, the inner cavity of the hollow structure facilitates the suppressed volumetric stress and increased contact between the electrode materials and electrolyte, in favor of structural integrity and prolonged cycling stability of active material [36]. Figure 2(f) presents the high-magnification TEM (HRTEM) image, where the contiguous lattice fringes with an interplanar distance of 0.47 nm can be indexed to the (111) crystal plane of LMO. Disordered regions in the carbon layer induced by carbon defects are also visible, indicating the successful heteroatom doping [37]. Additionally, as depicted in figure 2(g), the ring-like selected area electron diffraction (SAED) pattern with conspicuous diffraction rings correspond to the (111), (311), and (400) facets of $LiMn_2O_4$ in O_V-LMO@FOC. HAADF scanning TEM (HAADF-STEM) and elemental mapping images demonstrate the existence and uniformity of Mn, O, F, and C (figure 2(h)). To precisely visualize the oxygen vacancies in the $LiMn_2O_4$ lattice, the spherical aberration-corrected HAADF-STEM image of O_V-LMO@FOC is disclosed in figure S6, where lattice distortion and atomic rearrangement triggered by oxygen vacancies are visible [25].

As disclosed in figure 3(a), the crystallographic configurations of LMO, O_V-LMO@OC, and O_V-LMO@FOC were confirmed by XRD patterns. The characteristic diffraction peaks can be identified as the cubic spinel $LiMn_2O_4$ phase (JCPDS Card No. 35–0782) with the $Fd\bar{3}m$ space group without impurity. Simultaneously, O_V-LMO@FOC characters have higher diffraction intensity, suggesting a higher degree of crystallinity than that of LMO and O_V-LMO@OC, corresponding to the Rietveld-refinement results (figures 3(b), S7 and table S1). Figure 3(c) schematically elaborates the crystallographic configuration of $LiMn_2O_4$, where the Li, Mn, and O are located at 8a, 16d, and 32e sites to construct the contractive MnO_6 octahedral unit and expansive LiO_4 tetrahedral environment. Especially, the ordered Mn_2O_4 edge-shared cages provide a three-dimensional open framework channel for lithium ion diffusion. According to the Raman spectra

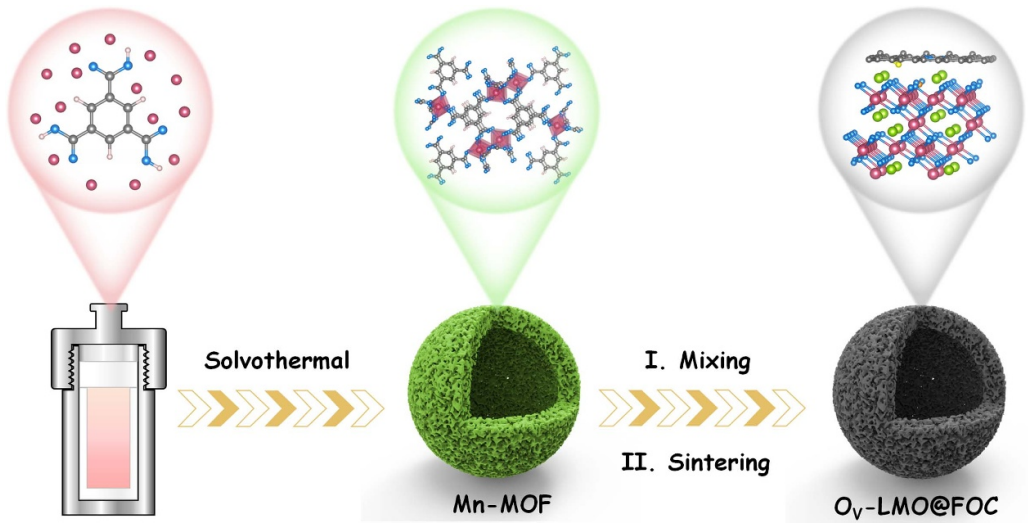

Figure 1. Schematic illustration of the synthetic strategy for hierarchical spinel $LiMn_2O_4$ cathode embedded in dual-heteroatom-doped carbon.

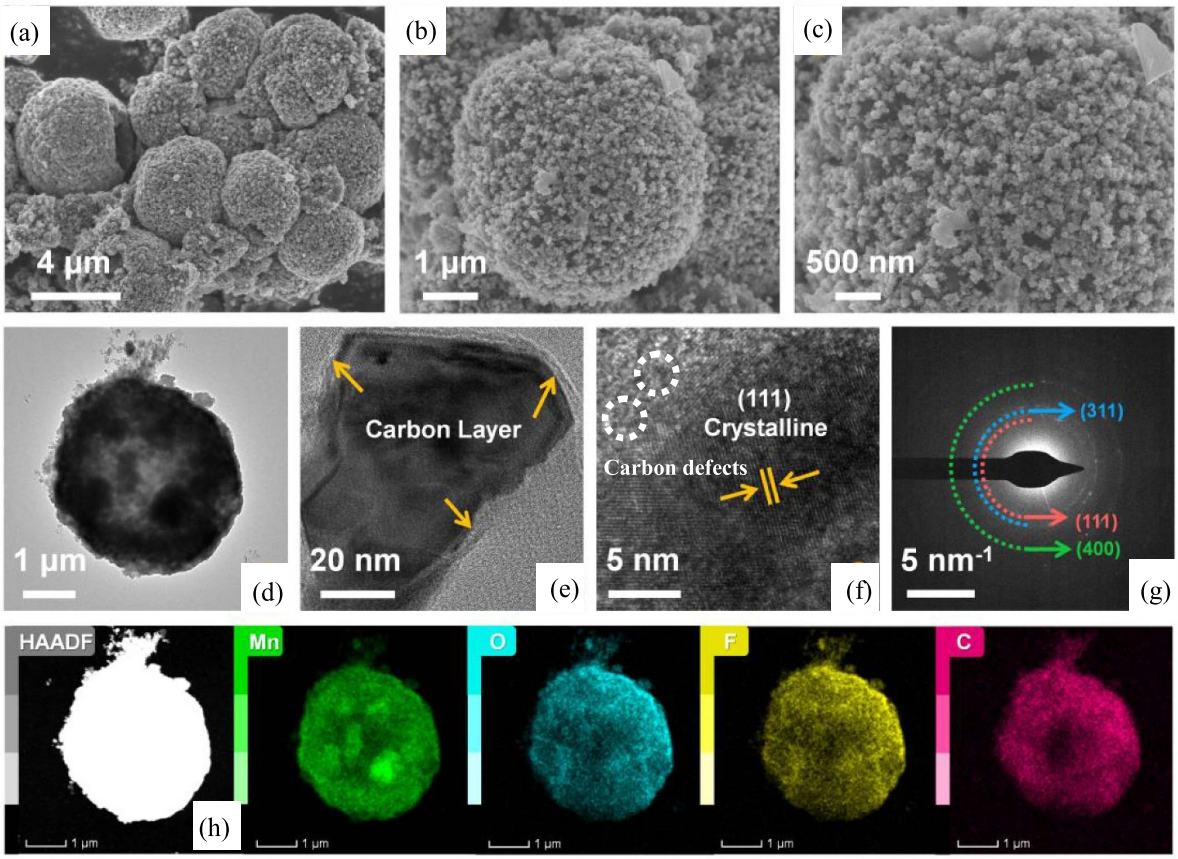

Figure 2. (a)–(c) SEM images of O_V-LMO@FOC. (d), (e) TEM images, (f) HRTEM image, (g) SAED pattern, and (h) HAADF-STEM and the relative elemental mapping images for Mn, O, F, and C of O_V-LMO@FOC.

(figure 3(d)), a vibration peak centered at around 626 cm^{-1} is designated to the Raman-active modes for $LiMn_2O_4$ phase, and two representative bands appeared at around 1336 and 1593 cm^{-1} are correlated with the disordered sp^3 carbon (D-band) and graphitic sp^2 carbon (G-band), respectively. The D and G band intensity ratios (I_D/I_G) for O_V-LMO@OC and O_V-LMO@FOC are 0.92 and 1.1, respectively, manifesting that fluoridation modification induces more defective sites in the carbon matrix [37]. The Raman spectra preliminarily substantiate the higher disordered degree caused

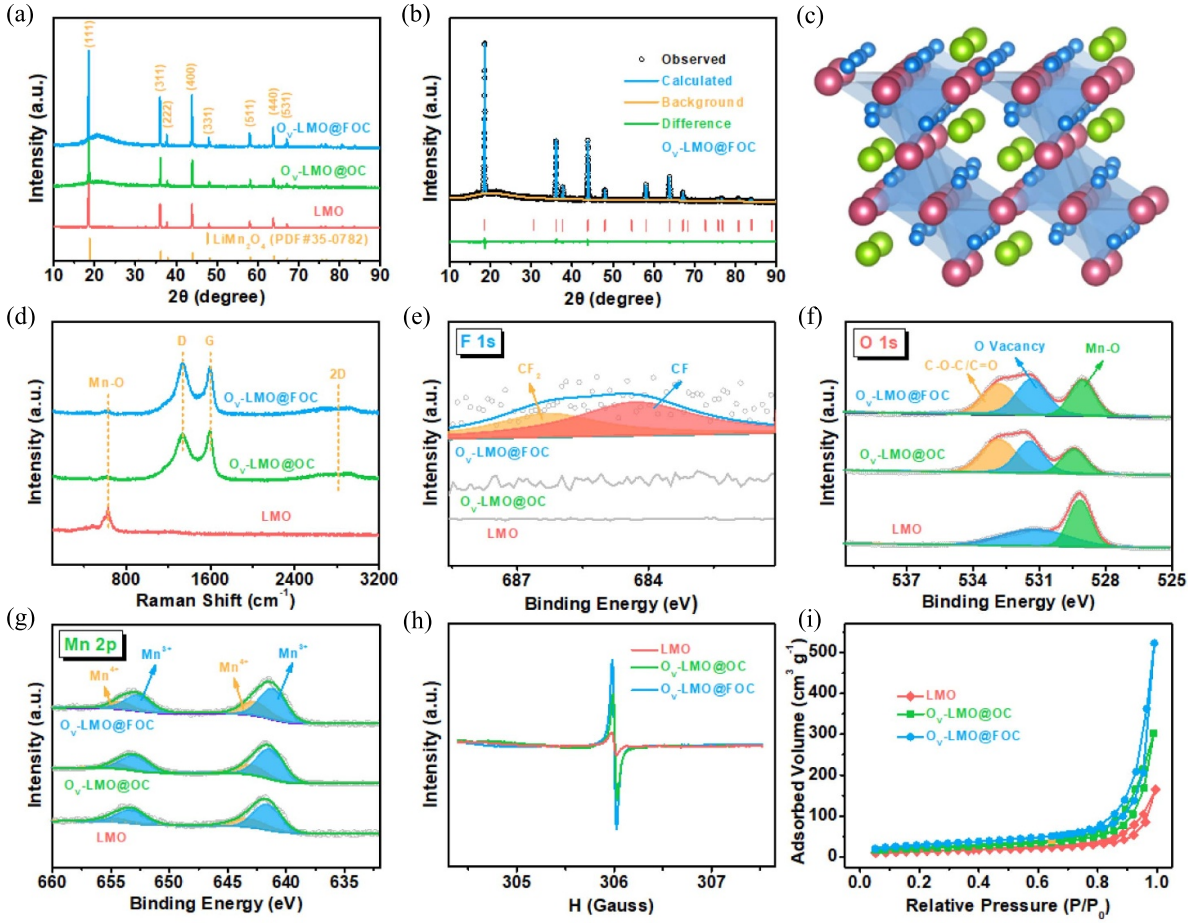

Figure 3. (a) XRD patterns of the as-synthesized LMO, O_V-LMO@OC, and O_V-LMO@FOC. (b) Rietveld refinement of the O_V-LMO@FOC. (c) Schematical illustration for the crystal structures of spinel $LiMn_2O_4$. (d) Raman spectra of the LMO, O_V-LMO@OC, and O_V-LMO@FOC. High-resolution XPS spectra of (e) F 1 s, (f) O 1 s, and (g) Mn 2p. The (h) EPR spectra and (i) nitrogen de/adsorption isotherms of the as-prepared LMO, O_V-LMO@OC, and O_V-LMO@FOC.

by fluorine doping, which can also be supported by the HRTEM observations. Furthermore, the electronic property of the electrode might be manipulated by both carbon layer and high electronegative fluorine/oxygen heteroatom-dopants, consequently propitious to the abundant lithium storage sites, boosted electronic conductivity, decreased transport resistances, and alleviated volumetric expansion upon (de)lithiation processes [24, 29]. Notably, the oxygen-deficient materials deliver lower peak intensity at 626 cm^{-1}, which is associated with the ameliorated electronic configuration and boosted electronic conductivity triggered by the introduction of oxygen defects [30, 31]. XPS spectra were implanted to investigate the chemical valence and bonding modes of the LMO, O_V-LMO@OC, and O_V-LMO@FOC. Figure S8 records the survey spectra that all the Li, Mn, O, C, and F elements coexist in the O_V-LMO@FOC samples. As the Li 1 s spectra elucidated in figure S9, the existence of lithium source for all samples demonstrates that successful sintering lithiation and transformation from the Mn-MOF into Li-integrated $LiMn_2O_4$, endowing the valid synthesis of LMO via the MOF-mediated strategy. Additionally, the F 1 s spectrum of O_V-LMO@FOC can be deconvoluted into two subpeaks of C−F (684.3 eV) and CF_2 (686.2 eV) bonds due to the F, O-dual-doped carbon matrix (figure 3(e)), conducive to the manipulation of electronic structure for O_V-LMO@FOC electrode [38]. The distribution of F-dopants inside the O_V-LMO@FOC was quantitatively investigated by Ar^+ etching-assisted XPS within a depth of 30 nm (figure S10), where the F 1 s peak of O_V-LMO@FOC varies due to the impact of Ar^+ etching treatment. As a result, the peak intensity of F disappears after Ar^+ etching down to 10, 20, and 30 nm. As mentioned earlier in TEM results, the carbon layer is ∼1.5 nm, which is much thinner than 10 nm. Therefore, the XPS spectra of F 1 s indicate that the F etches the carbon layer without penetrating into the LMO bulk. As depicted in figure 3(f), three O peaks are detected in the core-level O 1 s spectra in O_V-LMO@FOC and O_V-LMO@OC, while two peaks are available in the primitive LMO. The deconvoluted peaks at 533, 531.5, and 529.5 eV are ascribed to the existence of C–O–C or C=O, oxygen vacancy, and Mn–O, respectively, thereby indicating the successful doping of O into the carbon matrix and the introduction of oxygen vacancies [39]. Furthermore, the more pronounced characteristic peaks at 531.5 eV in O_V-LMO@FOC and O_V-LMO@OC indicate higher oxygen vacancy levels [30]. The

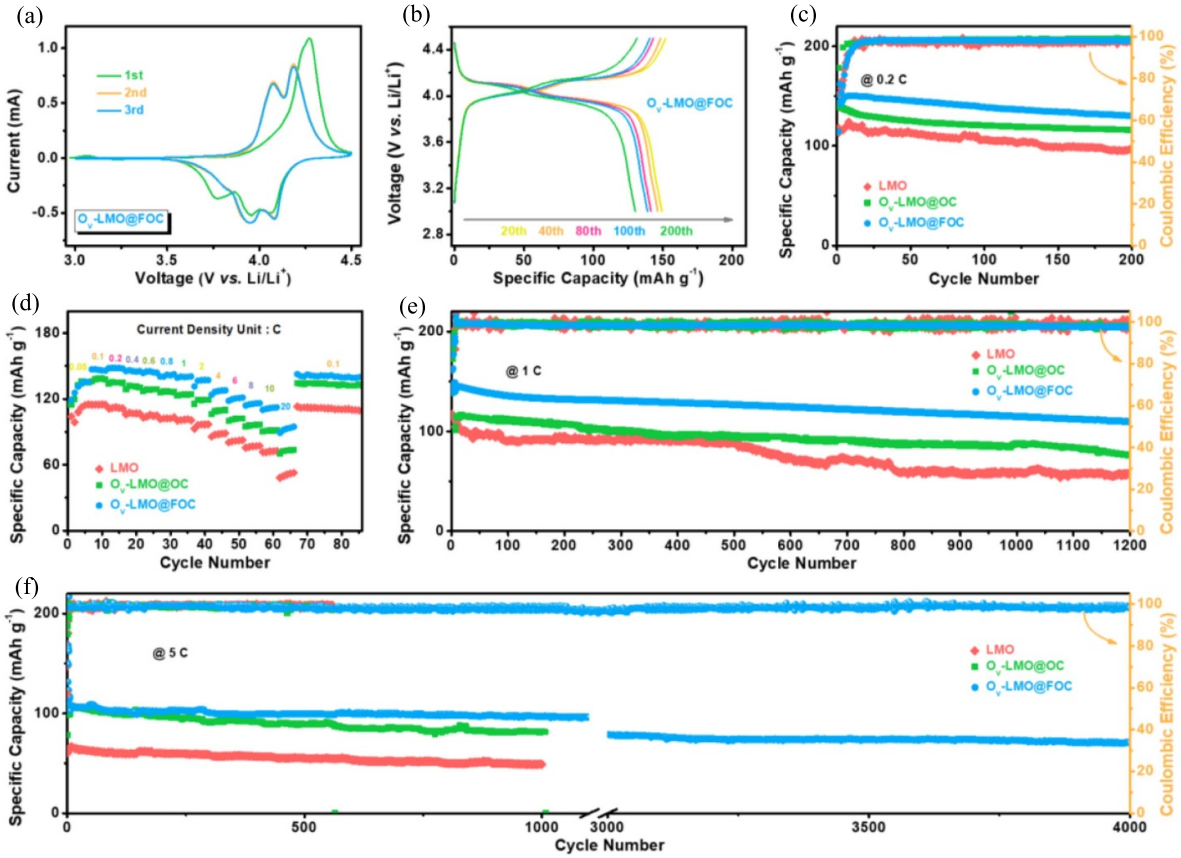

Figure 4. (a) The CV profiles with a scan rate of 0.1 mV s^{-1} of O_V-LMO@FOC cathode. (b) The galvanostatic charge/discharge curves at 0.2 C of O_V-LMO@FOC. (c) The cycling performance at 0.2 C, (d) rate capability at different current densities, and long-term cyclability at (e) 1 C and (f) 5 C for LMO, O_V-LMO@OC, and O_V-LMO@FOC cathodes, respectively.

fitting core-level Mn 2p spectra hold four characteristic sub-peaks, where the peaks with binding energies appeared at 642.8 and 654.2 eV are correlative with the Mn $2p_{3/2}$ and Mn $2p_{1/2}$ doublet for Mn^{4+}, and the peaks with binding energies appeared at 641.2 and 652.7 eV correlate to the Mn $2p_{3/2}$ and Mn $2p_{1/2}$ doublet for Mn^{3+} (figure 3(g)) [19]. To expound the oxygen vacancies, the electron paramagnetic resonance (EPR) spectra in figure 3(h) explicitly confirm the oxygen vacancies in both O_V-LMO@OC and O_V-LMO@FOC with respect to the oxygen vacancy signals at $g = 1.998$. This g-factor indicates the coexistence of Mn^{4+} and Mn^{3+} ions ($g = 1.98$ for sole LMO) leading to the shift of oxygen vacancy traits to lower g values [40]. Compared to O_V-LMO@OC, O_V-LMO@FOC bears the higher intensity and concentration of oxygen vacancy, which can boost the electronic conductivity by reconfiguring the electronic structure in $LiMn_2O_4$ crystal lattice and provide extra electrochemical active sites for lithium ion storage. Additionally, more diffusion pathways can be provided by vacancies for lithium ions to diffuse into the bulk. The N_2 sorption isothermal identifies the porosity nature (figure 3(i)), which the Brunauer–Emmett–Teller (BET) specific surface area takes up 48.4, 73.3, and 107.6 m^2 g^{-1} for LMO, O_V-LMO@OC, and O_V-LMO@FOC, respectively. Consequently, F-doping in carbon matrix can introduce the defective sites in the carbon framework, which is conducive to more active sites for charge storage. Additionally, the oxygen vacancies can increase the BET surface area with more lithium storage sites [41, 42], which can be ascribed to the surface reconstruction and lattice strain brought by the defect sites in the crystal structure. Herein, the F-doping and higher oxygen vacancy concentration contribute to higher BET surface area of O_V-LMO@FOC. Figure S11 discloses the pore-size distribution of all the samples featuring hierarchical micro-meso-macro-pores characteristics, which endows extra lithium storage sites, shortened diffusion channels, efficient electrolyte infiltration, and boosted charge diffusivity.

To comprehensively evaluate the electrochemical superiority of O_V-LMO@FOC, the as-synthesized cathode materials were assembled as cathodes in coin cells. Figure 4(a) depicts the CV profiles of O_V-LMO@FOC cathode with the voltage window of 3−4.5 V (vs. Li^+/Li), which holds two pairs of characteristic redox peaks at around 4.07/3.95 V and 4.18/4.08 V related to the single-phase transformation of $LiMn_2O_4/Li_{0.5}Mn_2O_4$ with Li−Li interaction and two-phase transformation of $Li_{0.5}Mn_2O_4/\lambda$-MnO_2 without Li−Li interaction, indicating the reversible (de)insertion of lithium ions from/into the tetrahedral sites of spinel structure by two-step conversion reactions, in which the lithium ion (de)insertion on

8a sites occurs at ∼4 V maintaining the cubic spinel symmetry [43, 44]. It is noteworthy that the single CV peak for initial cycle charge of O_V-LMO@FOC cathode may be attributed to the large polarization and the Li-poor phase of fresh O_V-LMO@FOC cathode, which the two-phase transformation of $Li_{0.5}Mn_2O_4/\lambda$-MnO_2 dominates at the 1st cycle charge. As the reversible (de)insertion proceeds, Li-poor phase transforms into Li-rich phase contributing to two typical redox peaks [45]. In all cases, the O_V-LMO@FOC bears much more symmetric redox peaks and higher peak currents than that of LMO and O_V-LMO@OC counterparts (figure S12). The CV profiles are superimposed since the second cycle onward, demonstrating the superior cycling reversibility of insertion and extraction of lithium ions. The minimized peak current of O_V-LMO@FOC upon the second cycle can be ascribed to the cycle aging of cathode. Additionally, no extra redox peak is observed in all samples, confirming that the oxygen vacancy does not change the crystal structure and the lithium storage mechanism of LMO. Figure 4(b) records the galvanostatic charge-discharge (GCD) curves at the current density of 0.2 C for O_V-LMO@FOC, which obviously features two potential plateaus at around 4.1 and 4.0 V concerning two peak pairs in the abovementioned CV results. Obviously, the O_V-LMO@FOC shows the superior discharge specific capacity than that of LMO and O_V-LMO@OC after the reversible 200th cycle course (figure S13). The corresponding cycling stability at 0.2 C is illustrated in figure 4(c), in which the O_V-LMO@FOC outperforms other counterparts with prosperous specific capacity of 130.2 mAh g^{-1} upon 200 cycles maintaining a capacity retention of 86.2%. It can be deduced that the enriched oxygen vacancy provides more extra electroactive sites and improves the practical electrode usage of O_V-LMO@FOC. Additionally, the Coulombic efficiency of the O_V-LMO@FOC approaches to ∼100% upon prolonged cycling, which the F, O-dual-doped carbonaceous surface modification effectively suppresses Jahn–Teller distortion and Mn dissolution induced by the direct contact between LMO and electrolyte, and thus contributing to the stable passivation membranes (cathode-electrolyte interphases, CEIs).

In the interim, the rate capability of O_V-LMO@FOC from low (0.05 C) to ultrahigh (20 C) rates is elaborated in figure 4(d). Plainly, the discharge capacity of O_V-LMO@FOC exceeds that of LMO and O_V-LMO@OC counterparts, with conspicuous capacity of 146, 147.8, 145.3, 144.3, 140.5, 140, 137.2, 127.6, 120.4, 115.9, and 111.7 mAh g^{-1} at the upgrading current density of 0.1, 0.2, 0.4, 0.6, 0.8, 1, 2, 4, 6, 8, and 10 C, respectively. Even under the harsh current condition of 20 C, the O_V-LMO@FOC achieves a brilliant discharge capacity of 93.7 mAh g^{-1}, superior to that of LMO (49.8 mAh g^{-1}) and O_V-LMO@OC (72.2 mAh g^{-1}). As the current density goes back to 0.1 C, O_V-LMO@FOC maintains its initial capacity value, endowing the reversibility and superiority of lithium storage. The exceptional rate capability of O_V-LMO@FOC could be associated with oxygen vacancy-induced boosted electronic conductivity and pseudocapacitive-controlled storage, as well as conductive F, O-dual-doped carbon matrix for elastic buffer layer for ameliorated structural disintegrity under high current density, which further facilitates the fast diffusion kinetics.

Figures 4(e) and (f) illuminate the prolonged cycle performances at 1 C and 5 C for LMO, O_V-LMO@OC, and O_V-LMO@FOC cathodes, respectively. Impressively, O_V-LMO@FOC features an inciting long-term cyclability of 112.5 mAh g^{-1} with 77.6% capacity retention at 1 C after 1200 cycles (figure 4(e)), which is much higher than those of LMO (58 mAh g^{-1} with capacity retention of 54.2%) and O_V-LMO@OC (76.1 mAh g^{-1} with capacity retention of 66.6%). Furthermore, the high-temperature cycle performances under 55 °C were investigated at the current rate of 1 C (Fig. S14), in which the O_V-LMO@FOC shows superior electrochemical performance than that of LMO and O_V-LMO@OC. The O_V-LMO@FOC shows a distinguished long-term cyclability of 119.8 mAh g^{-1} with 74.4% capacity retention at 1 C after 1000 cycles, much higher than that of LMO (66.2 mAh g^{-1}) and O_V-LMO@OC (105.7 mAh g^{-1}). Even at the ultrahigh current density of 5 C, the O_V-LMO@FOC bears a brilliant capacity of 96.9 mAh g^{-1} upon 1000 cycles with an extraordinary capacity retention of 90.7%, and maintains the discharge capacity of 70.9 mAh g^{-1} after 4000 cycles, manifesting the longevous cyclic stability and reversibility. However, severe capacity deterioration can be observed for both LMO (49.1 mAh g^{-1}) and O_V-LMO@OC (81.5 mAh g^{-1}) after 1000 cycles at 5 C, which highlights the benefits from both structural optimization of micro-/nano- multiscale structure and compositional optimization of surface modification and vacancy engineering. In brief, the distinguished electrochemical performance of O_V-LMO@FOC can be credited to synergistic effects in what follows. (I) The O_V considerably boosts electronic conductivity, provides extra electroactive sites, suppresses structural deformation, increases pseudocapacitive storage, and minimizes energy barrier upon reversible cycling, consequently inducing boosted diffusion kinetics, improved discharge capacity, as well as fabulous cycling stability and rate capability [46, 47]. (II) The F, O-dual-doped carbon matrix facilitates the overall conductivity of the electrode, mitigates electroactive particle agglomeration, immobilizes the structure expansion, and impedes the direct contact between LMO and corrosive electrolyte by jeopardizing Mn^{3+} disproportionation and Jahn–Teller effect, thus contributing to the structural stability towards long-term endurance [48]. (III) The multi-hierarchy hollow micro-/nano-structure offers extra electroactive sites and diffusion pathways by the inner surfaces of cavity, and relieves electrode polarization by the direct Li^+ diffusion in outer shells instead of diffusion from outer shells to inner cores [49]. Nevertheless, the hierarchical secondary micro-/nano-structure can effectively alleviate the volume expansion stress by the hollow cavity and secondary nanobuilding block, where the stress-release behavior optimizes the structural integrity for long-term cycling and rate performance [50, 51]. To examine the structural integrity during cycling, the SEM image of O_V-LMO@FOC after 4000 cycles at 5 C is disclosed in Fig. S15, where mechanical cracks and can hardly be detected and the primitive particle morphology is

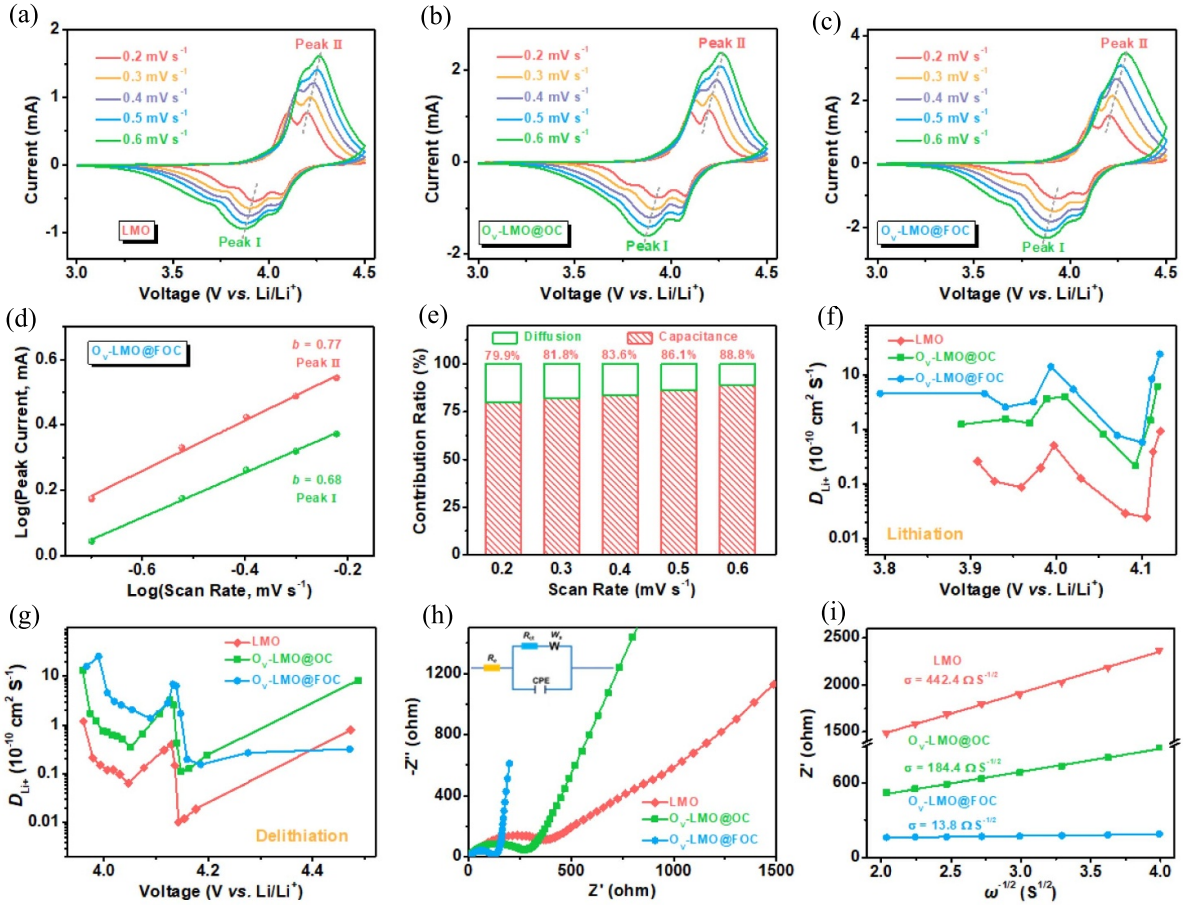

Figure 5. CV curves of (a) LMO, (b) O_V-LMO@OC, and (c) O_V-LMO@FOC at different scan rates increasing from 0.2 to 0.6 mV s^{-1} for quantitative kinetics analysis of the pseudocapacitive contribution. (d) The fitting *b* values of main cathodic (I) and anodic (II) peaks, and (e) pseudocapacitive contribution at different scan rates. The calculated Li^+ diffusion coefficients upon (f) lithiation, and (g) delithiation of LMO, O_V-LMO@OC, and O_V-LMO@FOC electrodes by GITT analysis. (h) The Nyquist plots (inset: equivalent circuit diagram) and (i) corresponding fitting relationship of Z' and $\omega^{-1/2}$ for LMO, O_V-LMO@OC, and O_V-LMO@FOC cathodes, respectively.

well retained, thereby indicating the stress-release effect of the heteroatom-doped carbon matrix. Benefitting from the pronounced structural/compositional optimizations, the rate capability and cycling property of O_V-LMO@FOC outperform presently reported LMO-based cathodes in LIBs, as illustrated in figure S16 and table S2.

As for the lithiation process, there are two lithium storage kinetics contributing to the total storage capacity: (a) numerous Li^+ ions adsorb around the surface of the F, O-dual-doped carbonaceous layer and negative electrons theoretically accumulate on the opposite interface of the carbon layer resulting in a typical electric double layer capacitor for exceptional specific capacity (termed as pseudocapacitive-dominant mechanism) [51]; (b) another part of Li^+ ions diffuse through the F, O-dual-doped carbonaceous layer and electrochemically participate in the reversible (de)insertion of lithium ions from/into the tetrahedral sites of $LiMn_2O_4$ spinel structure by two-step conversion reactions (denoted as diffusion-controlled mechanism) [43, 44]. To quantitative study the boosted diffusion kinetics of O_V-LMO@FOC cathode, figures 5(a)–(c) record the CV profiles at different scan rates to identify the pseudocapacitive contribution for lithium storage kinetics. Obviously, the CV profiles bear similar shape with upgrading current intensity upon scan rates varying from 0.2 to 0.6 mV s^{-1}. To differentiate the pseudocapacitive contribution ratio, the peak current (i) was logarithmically fitted against the scan rates (v) using the equation of $i = av^b$ [52]. It is acknowledged that a pseudocapacitive-dominant or diffusion-controlled mechanism can be observed when the value of b quals to 1 or 0.5, respectively. As depicted in figure 5(d), the b values of O_V-LMO@FOC (0.68 for cathodic peak and 0.77 for anodic peak) confirm that the pseudocapacitive-dominant and diffusion-controlled mechanisms concurrently contribute to the lithium storage course, which are higher than those of LMO (0.54 for cathodic peak and 0.67 for anodic peak, figure S17)(a)) and O_V-LMO@OC (0.66 for cathodic peak and 0.67 for anodic peak, figure S18(a)). Furthermore, the pseudocapacitive contribution ($k_1\nu$) and the diffusion-controlled contribution ($k_2\nu^{1/2}$) can be quantitatively separated by the law of $i(V) = k_1\nu + k_2\nu^{1/2}$ [52]. The pseudocapacitive contribution proportion takes up 86.1% at 0.5 mV s^{-1} for O_V-LMO@FOC (figure S19). The pseudocapacitive contribution ratios of O_V-LMO@FOC increases as the scan rates increase (from 79.9% to 88.8%, figure 5(e)). It is of note that the

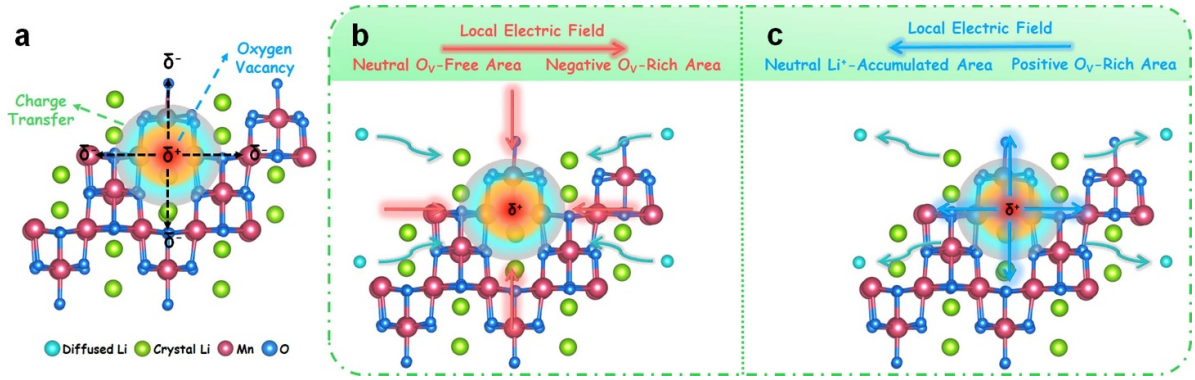

Figure 6. (a) The diagrammatic sketch of charge transfer phenomenon alongside O_V regime. The boosted lithium ion diffusivity mechanism induced by locally built-in electric fields upon (b) lithiation and (c) delithiation.

pseudocapacitive-dominant kinetics of O_V-LMO@FOC is larger than that of LMO (figure S17(c)) and O_V-LMO@OC (figure S18(c)). It may be attributed to the abundant oxygen vacancy and elastic F, O-dual-doped carbon matrix for pseudocapacitive storage, boosted electronic conductivity, large specific surface area, and extra active sites towards the fabulous rate capability of O_V-LMO@FOC.

Simultaneously, the lithium-ion diffusion coefficient (D_{Li+}) of O_V-LMO@FOC was investigated by the galvanostatic intermittent titration technique (GITT) [53], as portrayed in figure S20. The detailed calculation method of the D_{Li+} value was depicted in figure S21. Figures 5(f) and (g) illustrate the D_{Li+} value of all the LMO, O_V-LMO@OC, and O_V-LMO@FOC electrodes upon lithiation and delithiation processes, respectively. It can be observed in the D_{Li+} profiles with a sharp drop upon the (dis)charge voltage platform section and an increase upon depth (dis)charge stage. Usually, structural/phase transformations occur upon platform region with complex redox reactions, leading to an abnormal D_{Li+} [54]. Distinctly, as the (de)lithiation proceeds, the calculated D_{Li+} value for O_V-LMO@FOC is numerically higher than that of LMO and O_V-LMO@OC, demonstrating that the doping F in carbon matrix and oxygen vacancy could facilitate the boosted diffusion kinetics. Figure 5(h) presents the EIS analysis to study the resistance for interfacial reactions. The Nyquist plots are composed by depressed semicircles in the high- and medium-frequency regime related to the charge-transfer resistance (R_{ct}), and oblique line in low-frequency regime corresponded to the Warburg impedance (W_s) for lithium ion diffusion [55]. Accordingly, the O_V-LMO@FOC bears smaller R_{ct} and W_s than those of LMO and O_V-LMO@OC, affirming fast charge transfer and lithium ion diffusion kinetics of O_V-LMO@FOC. The heteroatom-doped carbon matrix constitutes a successive conductive network, while oxygen vacancies modulate the local charge distribution, thereby favoring the overall electron transportation [23, 25, 29]. Therefore, it can be credited with the modulation of electronic conductivity induced by the F, O-dual-doped carbonaceous matrix and oxygen vacancies. Simultaneously, the D_{Li+} value can be calculated by the relationship of $D_{Li+}=R^2T^2/2A^2n^4F^4c^2\sigma^2$, where the Warburg coefficient (σ) is in inverse proportion to the D_{Li+} in low frequency regime [56]. Consistent with the GITT results, the O_V-LMO@FOC features the lowest σ value (13.8) than that of LMO (442.4) and O_V-LMO@OC (184.4), whereas O_V-LMO@OC endows the highest D_{Li+} (figure 5(i)).

Figure 6 comprehensively deepens the boosted lithium-ion diffusivity and fabulous rate capability of O_V-LMO@FOC. In terms of the primitive $LiMn_2O_4$ crystal lattice, it can be observed the conducive charge transfer phenomenon and lopsided imbalanced charge distribution alongside the O_V regime (figure 6(a)), which synchronously incurs the surrounding atoms skewing ascribed to the oxygen defects, further inducing a positively charged regime in the oxygen vacancy center and an inversely negative region alongside the O_V center [57]. Whilst, the spontaneous formation of the locally built-in electric field around oxygen vacancy centers is commensurate with the Coulomb attractive force towards boosting lithium-ion diffusivity and thus kinetically facilitating rate performance. Upon lithiation course, the local electric field by pointing from the O_V-free region to the negatively charged region expedites the lithium-ion diffusion and leads to Li^+-agglomerated regime alongside the vacancy sites, as depicted in figure 6(b). The primitive negatively charged region will bear the electric neutrality as fully discharging. When the delithiation proceeds (figure 6(c)), the lithium ions migration is facilitated by the secondary local electric field directing from the positively charged region in the vacancy regime to the electroneutral lithiation region. Intriguingly, it can be expounded that the oxygen vacancy induced in-plane built-in electric field with the *in-situ* Li^+ migratory engineering is indispensable for boosting Li^+ diffusivity for superior rate capability.

DFT calculation was employed to unveil the synergistic effect on the superior electrochemical performance of O_V-LMO@FOC. The optimized geometric models of LMO, LMO@C, LMO@FC, LMO@OC, LMO@FOC, and O_V-LMO@FOC are shown in figure S22–S27, respectively. Figures 7(a)–(c) and S26 illustrate the density of states (DOS) together with the Fermi level (E_f), which reveals the electronic nature of the above-mentioned optimized models. The electronic property of LMO bulk behaves the discernible semiconductive characteristic with band-gap of 0.63 and 0.49 eV (figure 7(a)). Nevertheless, the band-gap decreases to 0.17 eV after combining the LMO with pure carbon (LMO@C) as shown in figure 7(b), which could be ascribed

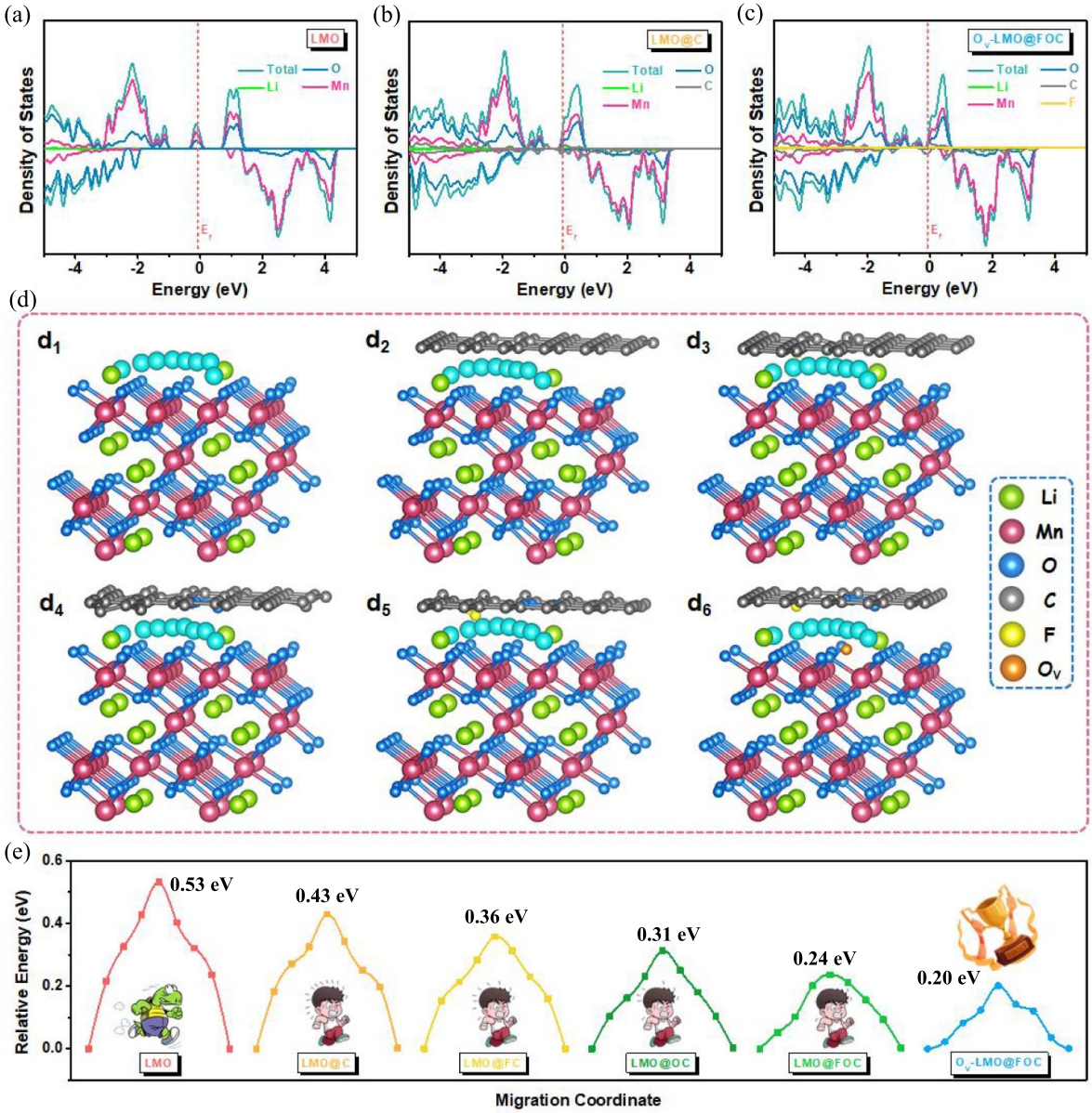

Figure 7. The DOS plots of (a) LMO, (b) LMO@C, and (c) O_V-LMO@FOC. The Fermi levels (E_f) are set to be 0 eV. (d) The calculated Li atom migration paths of LMO (d_1), LMO@C (d_2), LMO@FC (d_3), LMO@OC (d_4), LMO@FOC (d_5), and O_V-LMO@FOC (d_6) for Li atom migration alongside the depicted path, respectively. The optimized Li atom migration paths are indicated by series of aquamarine spheres. (e) The corresponding Li atom migration energy barrier curves.

to the electronic conductivity of carbon. As the carbon doped with F and O, the metallicity of LMO@FC, LMO@OC, LMO@FOC, and O_V-LMO@FOC samples can be observed along with the conspicuous and continuous E_f through the conduction bands, as well as the band-gap gradually dissipates (figures 7(c) and S28), where the most electronegative F ($\chi = 3.98$) and O ($\chi = 3.44$) heteroatoms can in-depth regulate the surface defects and electron structure to decrease the interfacial resistance and induce more available active electrons in the carbon coated heterostructure, further facilitating boosted electronic conductivity [58]. It is of note that the introduction of F and O dual-dopants in carbonaceous matrix induce the much denser DOS around the Fermi level, confirming that the F and O dual-dopants and conductive carbon are conducive to the boosted electronic conductivity of electrode materials. Additionally, the conduction bands of O_V-LMO@FOC are predominantly composed of Mn 3d states, while the valence bands are prominently taken up by C 2p, O 2p, and F 2p states. Consequently, O_V-LMO@FOC exerts a considerable effect on improved electronic conductivity comparable to that of LMO, thus contributing to the boosted Li^+ diffusion kinetic and prominent electrochemical capability.

The Li atom migration mechanism and corresponding migration paths are presented in figures 7(d) and S29, where the boosted Li atom diffusivity contributes to extraordinary rate capability [59]. To investigate the explicit role of oxygen vacancy and F, O-dual-doped carbonaceous matrix, the Li atom migration path that diffuses along the interface

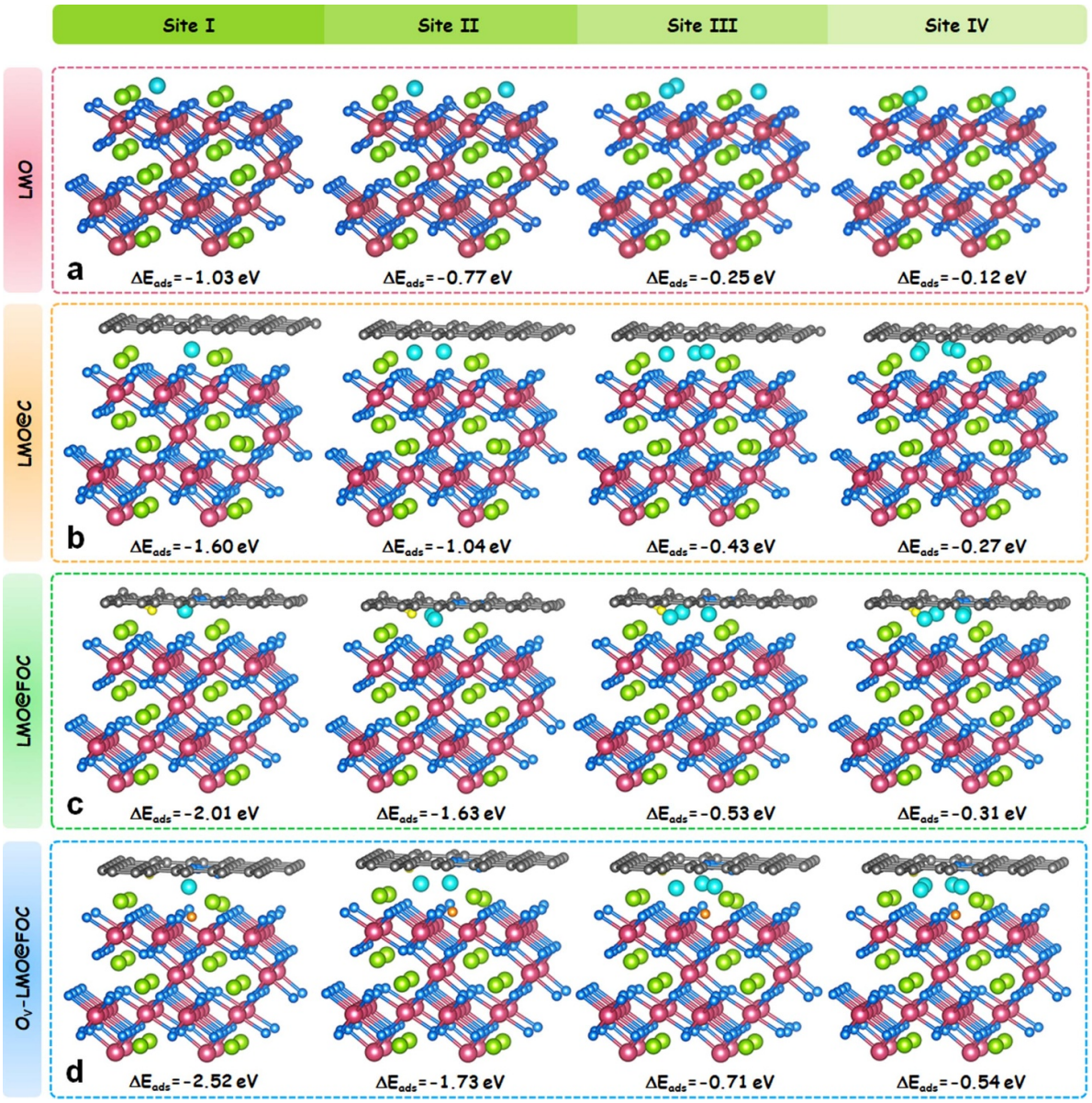

Figure 8. The different lithium ion adsorption sites alongside the side views and corresponding adsorption energies for (a) LMO, (b) LMO@C, (c) LMO@FOC, and (d) O_V-LMO@FOC, respectively.

between F, O-dual-doped carbonaceous matrix and LMO bulk were considered and is schematically depicted in the structural models of LMO, LMO@C, LMO@FC, LMO@OC, LMO@FOC, and O_V-LMO@FOC (figure 7(d)). The diffusion energy curves in figure 7(e) endow the migration energy barrier of LMO@C (0.43 eV) is distinctly lower than that of LMO bulk (0.53 eV), illustrating the optimized migration barriers and boosted migration kinetics of electrode by carbonaceous encapsulation. Moreover, migration energy barrier gradually decreases as F and O dual-doped into the carbon matrix (0.36 eV for LMO@FC, 0.31 eV for LMO@OC, 0.24 eV for LMO@FOC), indicating the high electronegativity of F is energetically favorable for accelerating electrode/electrolyte interactions by surface functionalization of carbon [60]. In addition, the C−F and C−O covalent bonds improve the electrode wettability and electrolyte permeation, further endowing accelerated charge migration [37]. Interestingly, by introducing the oxygen vacancy into the LMO bulk, the migration energy barrier of O_V-LMO@FOC (0.20 eV) is superior to that of LMO@FOC (0.24 eV), demonstrating that the introduction of O_V induces the local built-in electric field and confers the boosted lithium ion diffusivity and decreased energy barrier upon repeated (de)lithiation course, further decisive for fabulous rate capability.

The adsorption energies (ΔE_{ads}) with different amounts of lithium ion were systematically investigated to reveal the F, O-dual-doped carbonaceous matrix and oxygen vacancy induced distinguished lithium storage mechanism. Four possible Li adsorption conditions of LMO bulk (figures 8(a) and S30) models were considered, including one/two/three/four Li

ions adsorb on the intralayer of LMO bulk as Site I/II/III/IV, respectively. Likewise, there are our possible Li adsorption conditions of LMO@C (figures 8(b) and S31), LMO@FOC (figures 8(c) and S32), and O_V-LMO@FOC (figures 8(d) and S33) similar to the Li adsorption sites of LMO bulk. Upon the Li adsorbs on Site I, II, II, and IV, the adsorption energies of O_V-LMO@FOC are observed as −2.52, −1.73, −0.71, and −0.54 eV, respectively, which outperforms than those of LMO@C (−1.60 eV for Site I, −1.04 eV for Site II, −0.43 eV for Site III, and −0.27 eV for Site IV, respectively) and LMO@FOC (−2.01 eV for Site I, −1.63 eV for Site II, −0.53 eV for Site III, and −0.31 eV for Site IV, respectively); whereas those of LMO bulk are observed as −1.03, −0.77, −0.25, and −0.12 eV, accordingly. As recorded in figure S34, the adsorption energies of various adsorption sites of O_V-LMO@FOC conformably increase at corresponding adsorption sites, highlighting that the synergistic effect on oxygen vacancy and F, O-dual-doped carbonaceous matrix is energetically favorable for Li^+ adsorption and contributes to extra lithium ion active sites and boosted diffusion kinetics. Systematically, the FOC layer and oxygen vacancy are conducive to manipulate the electronic property of materials, exalt electrical conductivity, along with energetically favor Li^+ adsorption, further boosting diffusion kinetics and rate performance. To further support the practicability of the O_V-LMO@FOC cathode, commercial graphite was employed as the anode to assemble LIB full cells. As illustrated in figure S35, the as-assembled full cell exhibited satisfactory stability at 1 C (110.2 mAh g^{-1} with 87.7% capacity retention after 150 cycles), thereby indicating the feasibility and compatibility of the O_V-LMO@FOC cathode in practical battery systems [61, 62].

4. Conclusions

In closing, by means of MOF chemistry and anionic defect engineering, we have successfully developed hierarchical F, O-dual-doped carbon embedded oxygen vacancy enriched $LiMn_2O_4$ as longevous cycling-stable cathode. The O_V-LMO@FOC achieves distinguished electrochemical properties concerning exceptional specific capacity (130.2 mAh g^{-1} at 0.2 C after 200 cycles), prosperous rate capability (93.7 mAh g^{-1} even at 20 C), pre-eminent long-term cyclability (112.5 mAh g^{-1} after 1200 cycles with 77.6% capacity retention), and ultralong cycling stability (even at 5 C, 96.9 mAh g^{-1} upon 1000 cycles with a compelling capacity retention of 90.7%, and 70.9 mAh g^{-1} upon 4000 cycles). Unraveled by experimental and theoretical implementations, both oxygen vacancy and F, O-dual-doped carbon reconfigure the electronic structure of O_V-LMO@FOC, endowing enhanced electronic conductivity, tremendous active centers, expedited diffusion kinetics, easy Li^+ adsorption, and suppressed Mn dissolution in the electrolyte, further achieving unparalleled rate capability and ultralong cyclability. This work broadens horizons for meticulous engineering for MOF-chemistry in surface modification and electronic modulation towards longevous cycling-stable cathode materials.

5. Future perspectives

Spinel $LiMn_2O_4$ (LMO) is a promising candidate as the commercial LIB cathode material due to its enticing merits including considerable economic efficiency, nontoxicity, high operating voltage, and satisfactory energy/power density. Nevertheless, LMO still encounters some tricky issues including Jahn–Teller effect related to Mn^{2+} dissolution and low electrical conductivity. To promote its adaptation to practical LIBs and strengthen its competitive edge in the LIB industry, future research efforts should be dedicated to the versatile micro-/nano-structural design with the balanced merit of micro and nano structures, for which the self-sacrificial templated route is viable for directional fabrication. Simultaneously, compositional optimization without devastating the primitive spinel structure and sacrificing the overall energy density is necessary. With this aim, surface modification with proper mass/volume ratios of carbonaceous layers can immobilize the bulk structure towards strengthened structural integrity, establish successive conductive networks for unimpeded charge transfer, and provide more lithium storage city for enhancing rate capability, accompanied by the minimized sacrifice in mass/volume energy densities to warrant its feasibility in practical LIBs. Furthermore, atomic-level modification including electronegative atom doping and oxygen vacancy engineering are favorable for the manipulation of electronic configuration towards boosted electronic/ion conductivity.

Data availability statement

Data is available at the supplementary file.

Acknowledgment

We gratefully acknowledge the financial support from the Open Fund of Energy and Materials Chemistry Joint Laboratory of SCNU and TINCI, China (SCNU-TINCI-202207). We would like to thank Shiyanjia Lab (www.shiyanjia. com) for the XPS analysis. This work was financially supported by the Natural Science Foundation of China (No. 52302283).

Author contributions

Jia Lin: Data curation. Wanxin Mai, Xiaomeng Lu, Hao Li, Xiaohong Tan: Formal analysis. Yongbo Wu, Yuhong Luo: Investigation. Xiaoming Lin, Chao Yang, Yong Wang: Supervision. Xiaoming Lin: Funding acquisition. Shuangqiang Chen: Methodology. Chao Yang: Funding acquisition.

Conflict of interest

The authors declare that they have no known competing financial interests or personal relationships that could have appeared to influence the work reported in this paper.

ORCID iD

Xiaoming Lin https://orcid.org/0000-0001-8835-103X

References

[1] Huang M Y, Xu Z G and Lin X M 2024 Mechanistic analysis of Co_2VO_4/X (X = Ni, C) heterostructures as anode materials of lithium-ion batteries *Chin. J. Struct. Chem.* **43** 100309

[2] Park C Y, Kim J, Lim W G and Lee J W 2024 Toward maximum energy density enabled by anode-free lithium metal batteries: recent progress and perspective *Exploration* **4** 20210255

[3] Wang Y, Xu C X, Tian X T, Wang S Y and Zhao Y 2023 Challenges and modification strategies of high-voltage cathode materials for Li-ion batteries *Chin. J. Struct. Chem.* **42** 100167

[4] Tang L, Cheng X P, Wu R, Cao T C, Lu J X, Zhang Y F and Zhang Z 2022 Monitoring the morphology evolution of $LiNi_{0.8}Mn_{0.1}Co_{0.1}O_2$ during high-temperature solid state synthesis via *in situ* SEM *J. Energy Chem.* **66** 9–15

[5] Li W D, Erickson E M and Manthiram A 2020 High-nickel layered oxide cathodes for lithium-based automotive batteries *Nat. Energy* **5** 26–34

[6] Duffner F, Kronemeyer N, Tübke J, Leker J, Winter M and Schmuch R 2021 Post-lithium-ion battery cell production and its compatibility with lithium-ion cell production infrastructure *Nat. Energy* **6** 123–34

[7] Liu Y M, Li J Y, Xu F X, Li Y J, Zheng J C and He Z J 2022 The multiple modification road of Li-rich manganese-based cathode materials *Chin. J. Struct. Chem.* **41** 2209045–55

[8] Luo X H, Xing L D, Vatamanu J, Chen J W, Chen J K, Liu M Z, Wang C, Xu K and Li W S 2022 Inhibiting manganese (II) from catalyzing electrolyte decomposition in lithium-ion batteries *J. Energy Chem.* **65** 1–8

[9] Yang Z G, Zhang J L, Kintner-Meyer M C W, Lu X C, Choi D W, Lemmon J P and Liu J 2011 Electrochemical energy storage for green grid *Chem. Rev.* **111** 3577–613

[10] Zhao H and Yuan Z Y 2021 Surface/interface engineering of high-efficiency noble metal-free electrocatalysts for energy-related electrochemical reactions *J. Energy Chem.* **54** 89–104

[11] Huang Y M, Dong Y H, Li S, Lee J, Wang C, Zhu Z, Xue W J, Li Y and Li J 2021 Lithium manganese spinel cathodes for lithium-ion batteries *Adv. Energy Mater.* **11** 2000997

[12] Wu X Y, Yang Z S, Xu L, Wang J H, Fan L L, Kong F J, Shi Q F, Piao Y Z, Diao G W and Chen M 2022 Consecutive hybrid mechanism boosting Na^+ storage performance of dual-confined $SnSe_2$ in N, Se-doping double-walled hollow carbon spheres *J. Energy Chem.* **74** 8–17

[13] Shi R J, Jiao S L, Yue Q Q, Gu G Q, Zhang K and Zhao Y 2022 Challenges and advances of organic electrode materials for sustainable secondary batteries *Exploration* **2** 20220066

[14] Li S *et al* 2021 Thermally aged Li–Mn–O cathode with stabilized hybrid cation and anion redox *Nano Lett.* **21** 4176–84

[15] Hallot M, Nikitin V, Lebedev O I, Retoux R, Troadec D, De Andrade V, Roussel P and Lethien C 2022 3D $LiMn_2O_4$ thin film deposited by ALD: a Road toward high-capacity electrode for 3D Li-ion microbatteries *Small* **18** 2107054

[16] Kuenzel M, Kim G T, Zarrabeitia M, Lin S D, Schuer A R, Geiger D, Kaiser U, Bresser D and Passerini S 2020 Crystal engineering of $TMPO_x$-coated $LiNi_{0.5}Mn_{1.5}O_4$ cathodes for high-performance lithium-ion batteries *Mater. Today* **39** 127–36

[17] Zhang Y, Zhang J H, Li X Q, Chen G Y, Zhang B L, Liu H M, Wang Y G and Ma Z F 2022 Construction of AlF_3 layer to improve $Na_{3.12}Fe_{2.44}(P_2O_7)_2$ interfacial stability for high temperature stable cycling *Chem. Eng. J.* **430** 132708

[18] Lee S, Cho Y, Song H K, Lee K T and Cho J 2012 Carbon-coated single-crystal $LiMn_2O_4$ nanoparticle clusters as cathode material for high-energy and high-power lithium-ion batteries *Angew. Chem., Int. Ed.* **51** 8748–52

[19] Wang S, Ma W B, Sang Z Y, Hou F, Si W P, Guo J D, Liang J and Yang D A 2022 Dual-modification of manganese oxide by heterostructure and cation pre-intercalation for high-rate and stable zinc-ion storage *J. Energy Chem.* **67** 82–91

[20] Lee J *et al* 2018 Reversible Mn^{2+}/Mn^{4+} double redox in lithium-excess cathode materials *Nature* **556** 185–90

[21] Liu T C *et al* 2024 Zincophilic Sn sites induced the local ion enrichment for compact and homogenous growth of Zn biscuits in long-life Zn metal batteries *J. Mater. Chem.* A **12** 2283–93

[22] Yu X L, Deng J J, Yang X, Li J, Huang Z H, Li B H and Kang F Y 2020 A dual-carbon-anchoring strategy to fabricate flexible $LiMn_2O_4$ cathode for advanced lithium-ion batteries with high areal capacity *Nano Energy* **67** 104256

[23] Cao Y *et al* 2024 Steering lithium and potassium storage mechanism in covalent organic frameworks by incorporating transition metal single atoms *Proc. Natl Acad. Sci. USA* **121** e2315407121

[24] Wang L G, Liu T F, Wu T P and Lu J 2021 Exploring new battery knowledge by advanced characterizing technologies *Exploration* **1** 20210130

[25] Lu X M, Cao Y N, Sun Y, Wang H C, Sun W W, Xu Y, Wu Y, Yang C and Wang Y 2024 sp-carbon-conjugated organic polymer as multifunctional interfacial layers for ultra-long dendrite-free lithium metal batteries *Angew. Chem., Int. Ed.* **63** e202320259

[26] Feng W, Long P, Feng Y Y and Li Y 2016 Two-dimensional fluorinated graphene: synthesis, structures, properties and applications *Adv. Sci.* **3** 1500413

[27] Cai G R, Yan P, Zhang L L, Zhou H C and Jiang H L 2021 Metal–organic framework-based hierarchically porous materials: synthesis and applications *Chem. Rev.* **121** 12278–326

[28] Du R, Wu Y F, Yang Y C, Zhai T T, Zhou T, Shang Q Y, Zhu L H, Shang C X and Guo Z X 2021 Porosity engineering of MOF-based materials for electrochemical energy storage *Adv. Energy Mater.* **11** 2100154

[29] He Y N *et al* 2023 Lithiation-induced controllable vacancy engineering for developing highly active Ni_3Se_2 as a high-rate and large-capacity battery-type cathode in hybrid supercapacitors *J. Energy Chem.* **78** 37–46

[30] Hou X Y, Ruan M, Zhou L J, Wu J C, Meng B C, Huang W L, Zhong K A, Yang K, Fang Z and Xie K Y 2023 Superior lithium storage performance in MoO_3 by synergistic effects: oxygen vacancies and nanostructures *J. Energy Chem.* **78** 91–101

[31] Zhang T, Sun Z, Li S Y, Wang B J, Liu Y F, Zhang R G and Zhao Z K 2022 Regulating electron configuration of single Cu sites via unsaturated N,O-coordination for selective oxidation of benzene *Nat. Commun.* **13** 6996

[32] Blöchl P E, Först C J and Schimpl J 2003 Projector augmented wave method: ab initio molecular dynamics with full wave functions *Bull. Mater. Sci.* **26** 33–41

[33] Kresse G and Joubert D 1999 From ultrasoft pseudopotentials to the projector augmented-wave method *Phys. Rev.* B **59** 1758–75

[34] Hammer B, Hansen L B and Norskov J K 1999 Improved adsorption energetics within density-functional theory using revised Perdew-Burke-Ernzerhof functionals *Phys. Rev.* B **59** 7413–21

[35] Yeon J S, Ko Y H, Park T H, Park H, Kim J and Park H 2022 Multidimensional hybrid architecture encapsulating cobalt

oxide nanoparticles into carbon nanotube branched nitrogen-doped reduced graphene oxide networks for lithium–sulfur batteries *Energy Environ. Mater.* **5** 555–64
[36] Qin M L *et al* 2019 Optimization of Von Mises stress distribution in mesoporous α-Fe_2O_3/C hollow bowls synergistically boosts gravimetric/volumetric capacity and high-rate stability in alkali-ion batteries *Adv. Funct. Mater.* **29** 1902822
[37] Wang D *et al* 2021 High-yield production of non-layered 2D carbon complexes: thickness manipulation and carbon nanotube branches for enhanced lithium storage properties *J. Energy Chem.* **59** 19–29
[38] Xie J F, Zhao X T, Wu M X, Li Q H, Wang Y B and Yao J N 2018 Metal-free fluorine-doped carbon electrocatalyst for CO_2 reduction outcompeting hydrogen evolution *Angew. Chem., Int. Ed.* **57** 9640–4
[39] Wang H Q, Han J L, Li L X, Peng F, Zheng F H, Huang D Q, Lai F Y, Hu S J, Pan Q C and Li Q Y 2021 Effects of oxidized Ketjen Black as conductive additives on electrochemical performance of the $LiMn_2O_4$@Al_2O_3 cathode in lithium-ion batteries *J. Alloys Compd.* **860** 158482
[40] Venkataswamy P, Rao K N, Jampaiah D and Reddy B M 2015 Nanostructured manganese doped ceria solid solutions for CO oxidation at lower temperatures *Appl. Catal.* B **162** 122–32
[41] Zou Y H, Zhang W, Chen N, Chen S, Xu W J, Cai R S, Brown C L, Yang D J and Yao X D 2019 Generating oxygen vacancies in MnO hexagonal sheets for ultralong life lithium storage with high capacity *ACS Nano* **13** 2062–71
[42] Fang Y T, Cai W L, Zhu S S, Xu K L, Zhu M G, Xiao G N and Zhu Y C 2021 Vesicle-shaped ZIF-8 shell shielded in 3D carbon cloth for uniform nucleation and growth towards long-life lithium metal anode *J. Energy Chem.* **54** 105–10
[43] Xia Y Y and Yoshio M 1996 An investigation of lithium ion insertion into spinel structure Li-Mn-O compounds *J. Electrochem. Soc.* **143** 825–33
[44] Ding T L, Xie J A, Cao G S, Zhu T J, Yu H M and Zhao X B 2011 Single-crystalline $LiMn_2O_4$ nanotubes synthesized via template-engaged reaction as cathodes for high-power lithium ion batteries *Adv. Funct. Mater.* **21** 348–55
[45] Kim M, Jeong M, Yoon W S and Kang B 2020 Ultrafast kinetics in a phase separating electrode material by forming an intermediate phase without reducing the particle size *Energy Environ. Sci.* **13** 4258–68
[46] Warburton R E, Young M J, Letourneau S, Elam J W and Greeley J 2020 Descriptor-based analysis of atomic layer deposition mechanisms on spinel $LiMn_2O_4$ lithium-ion battery cathodes *Chem. Mater.* **32** 1794–806
[47] Ma X Q, Li Y D, Long X J, Luo H C, Xu C P, Wang G Z and Zhao W X 2023 Construction of phosphorus-doping with spontaneously developed selenium vacancies: inducing superior ion-diffusion kinetics in hollow Cu_2Se@C nanospheres for efficient sodium storage *J. Energy Chem.* **77** 227–38
[48] Zhang S, Deng W T, Momen R, Yin S Y, Chen J, Massoudi A, Zou G Q, Hou H S, Deng W N and Ji X B 2021 Element substitution of a spinel $LiMn_2O_4$ cathode *J. Mater. Chem.* A **9** 21532–50
[49] Li Q, Zhao Y H, Liu H D, Xu P D, Yang L T, Pei K, Zeng Q W, Feng Y Z, Wang P and Che R C 2019 Dandelion-like Mn/Ni Co-doped CoO/C hollow microspheres with oxygen vacancies for advanced lithium storage *ACS Nano* **13** 11921–34
[50] Zhang Z L *et al* 2019 Hollow multihole carbon bowls: a stress–release structure design for high-stability and high-volumetric-capacity potassium-ion batteries *ACS Nano* **13** 11363–71
[51] Chen J J, Ling M Y, Wan L Y, Chen C, Liu P, Zhang Q Y and Zhang B L 2022 The construction of molybdenum disulfide/cobalt selenide heterostructures @ N-doped carbon for stable and high-rate sodium storage *J. Energy Chem.* **71** 1–11
[52] Chen T T, Wang F F, Cao S, Bai Y, Zheng S S, Li W T, Zhang S T, Hu S X and Pang H 2022 *In situ* synthesis of MOF-74 family for high areal energy density of aqueous nickel–zinc batteries *Adv. Mater.* **34** 2201779
[53] Yang H, Zhou W H, Chen D, Liu J H, Yuan Z Y, Lu M J, Shen L F, Shulga V, Han W and Chao D L 2022 The origin of capacity fluctuation and rescue of dead Mn-based Zn–ion batteries: a Mn-based competitive capacity evolution protocol *Energy Environ. Sci.* **15** 1106–18
[54] Zhang Y B, Yin C, Qiu B, Chen G X, Shang Y and Liu Z P 2022 Revealing Li-ion diffusion kinetic limitations in micron-sized Li-rich layered oxides *Energy Storage Mater.* **53** 763–73
[55] Cai Y J, Wang W K, Cao X X, Wei L F, Ye C C, Meng C F, Yuan A H, Pang H and Yu C 2022 Synthesis of tostadas-shaped metal-organic frameworks for remitting capacity fading of Li-ion batteries *Adv. Funct. Mater.* **32** 2109927
[56] Chen F, Di Y, Su Q, Xu D, Zhang Y, Zhou S, Liang S, Cao X and Pan A 2023 Vanadium-modified hard carbon spheres with sufficient pseudographitic domains as high-performance anode for sodium-ion batteries *Carbon Energy* **5** e191
[57] Liu Y W *et al* 2017 Local electric field facilitates high-performance Li-ion batteries *ACS Nano* **11** 8519–26
[58] Shao Y, Zha Z T and Wang H 2021 Heteroatom-doped porous carbon-supported single-atom catalysts for electrocatalytic energy conversion *J. Energy Chem.* **63** 54–73
[59] Ye J H *et al* 2021 Oxygen vacancies enriched nickel cobalt based nanoflower cathodes: mechanism and application of the enhanced energy storage *J. Energy Chem.* **62** 252–61
[60] Yang J L, Ju Z C, Jiang Y, Xing Z, Xi B J, Feng J K and Xiong S L 2018 Enhanced capacity and rate capability of nitrogen/oxygen dual-doped hard carbon in capacitive potassium-ion storage *Adv. Mater.* **30** 1700104
[61] Zhou J-E, Liu Y, Peng Z, Ye Q, Zhong H, Lin X, Zeng R, Wu Y and Ye J 2024 Unveiling the tailorable electrochemical properties of zeolitic imidazolate framework-derived Ni-doped $LiCoO_2$ for lithium-ion batteries in half/full cells *J. Energy Chem.* **93** 229–42
[62] Zhou J-E, Li Y, Lin X and Ye J 2025 Prussian blue analogue-templated nanocomposites for alkali-ion batteries: progress and perspective *Nano-Micro. Lett.* **17** 9